

# Sub- $\mu\text{m}$ axial precision depth imaging with entangled two-color Hong-Ou-Mandel microscopy

Cyril Torre<sup>1,2</sup>, Alex McMillan<sup>1</sup>, Jorge Monroy-Ruz<sup>1</sup>, and Jonathan C. F. Matthews<sup>1</sup>

<sup>1</sup>Quantum Engineering Technology Labs, H.H. Wills Physics Laboratory and Department of Electrical & Electronic Engineering, University of Bristol, Tyndall Avenue, Bristol BS8 1FD, United Kingdom

<sup>2</sup>Quantum Engineering Centre for Doctoral Training, H.H. Wills Physics Laboratory and Department of Electrical & Electronic Engineering, University of Bristol, Tyndall Avenue, Bristol BS8 1FD, United Kingdom

(Received 10 January 2023; accepted 26 July 2023; published 24 August 2023)

The quantum interference of two wavelength-entangled photons overlapping at a beamsplitter results in an oscillating interference pattern. The frequency of the beat note is dependent on the wavelength separation of the entangled photons but is robust to wavelength scale perturbations that can limit the practicality of standard interferometry. Here we use two-color entanglement interferometry to evaluate the variation in thickness of a semi-transparent sample in combination with two-dimensional raster scanning. The axial precision and the dynamic range of the microscope are actively controlled by adjusting the wavelength separation of the entangled photon pairs. Sub- $\mu\text{m}$  precision is reported using up to 12.3 nm of detuning and  $\sim 10^4$  detected photon pairs.

DOI: [10.1103/PhysRevA.108.023726](https://doi.org/10.1103/PhysRevA.108.023726)

## I. INTRODUCTION

The Hong-Ou-Mandel (HOM) interference effect is routinely used in quantum photonics, for example, to generate NOON states for quantum-enhanced interferometry [1] and imaging [2,3], for photonic two-qubit quantum logic gates [4–6], and it is the underpinning physical phenomenon of optical quantum computational advantage experiments [7]. It is typically observed when two photons in separate temporal modes, but are otherwise indistinguishable, are made to overlap at a beamsplitter (Fig. 1). As the relative arrival time  $t$  of the two photons is reduced to zero, the detection rate of the photons exiting the beamsplitter on separate paths (antibunching) ideally drops to zero, while the proportion of detection events with photons output on the same path (bunching) increases. This can be used to measure a relative optical path length that induces  $t$ , which was demonstrated to subpicosecond precision in the seminal experiment by Hong, Ou, and Mandel [8].

For application of the HOM effect to imaging and sensing, more recent demonstrations have extracted higher sensitivities to measure  $t$  with attosecond precision [9], and have utilized the effect for polarization measurements [10], spectroscopy [11], multimode depth imaging [12], and refractive index measurement [13]. In these works, the Cramér-Rao bound (CRB) related the variance ( $\sigma_t^2$ ) to the Fisher information ( $\mathcal{F}(t)$ ) through the inequality  $\sigma_t^2 \geq 1/\mathcal{F}(t)$ . The limit of this bound quantifies the maximum achievable precision  $\sigma_t$  for an unbiased estimator measuring  $t$ .  $\mathcal{F}(t)$  can be modelled from analytic probability functions  $P_i(t)$  for each outcome ( $i$ )

using

$$\mathcal{F}(t) = \sum_{i=1}^n \frac{1}{P_i(t)} \left( \frac{\partial P_i(t)}{\partial t} \right)^2, \quad (1)$$

which highlights the dependence of the maximum precision bound on the shape of the interference features given by  $P_i(t)$ . For degenerate photons,  $\mathcal{F}(t)$  can be increased by broadening the photon spectrum to yield steeper HOM interference features [9]. However, increasing the bandwidth of

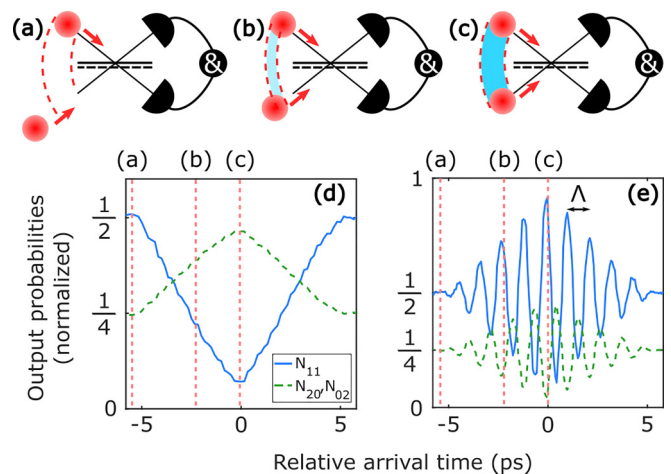


FIG. 1. HOM interference for degenerate and two-color entangled photons. (a)–(c) Photon pairs incident on a beamsplitter with (a) zero, (b) partial, and (c) complete temporal overlap. Typical resulting HOM interference patterns for (d) degenerate and (e) two-color entangled photons with a frequency beat note of 0.90 THz are plotted, showing bunching ( $N_{20}, N_{02}$ : green dashed) and antibunching ( $N_{11}$ : blue) rates. Overlap conditions corresponding to cases (a)–(c) are highlighted. The wavelength of the oscillating interference fringe  $\Lambda$  [marked on (e)] is directly controlled by the frequency detuning ( $\Delta\nu = 1/\Lambda$ ) of signal and idler wavelengths.

photons leads to a tradeoff between measurement precision and dynamic range, while highly broadband photons can also exacerbate complications arising from dispersion in the apparatus optics. While sensitivity to dispersion is addressed by some terahertz pulsed imaging techniques which are widely used in bio-imaging, these can suffer from other issues such as comparatively poor lateral and axial resolution [14–16]. More broadly, for many high-precision classical imaging techniques, such as super-resolution microscopy, the intensity of illumination required to achieve sub-micron level precision is between 8 and 12 orders of magnitude greater than the microscope proposed in this manuscript [17,18]. Consequently, the HOM microscope can reach a higher Fisher information per photon, which can be an important consideration for photo-sensitive samples and can otherwise be a limiting factor for measurement precision.

An alternative to increase HOM interferometer sensitivity is to use the two-color entangled state [19,20]

$$|\Psi\rangle = \frac{1}{\sqrt{2}}(|\nu_S\rangle_A |\nu_I\rangle_B + e^{i\phi(t)} |\nu_I\rangle_A |\nu_S\rangle_B), \quad (2)$$

where  $\nu_S$  and  $\nu_I$  label frequencies of the signal (horizontally polarized) and idler (vertically polarized) photons, while  $A$  and  $B$  denote the two separate optical paths that will overlap at a beamsplitter. The resulting two-photon interference of  $|\Psi\rangle$  exhibits a beat note with a frequency  $\Delta\nu = \nu_S - \nu_I$  that is dependent on the spectral detuning of signal and idler [19] (see Appendix A for the mathematical model employed). This approach was shown to directly modify  $\mathcal{F}(t)$  and was applied to detect temperature drifts in optical fiber [20]. To apply two-color HOM interferometry to depth imaging we construct a tunable wavelength-entangled photon pair source and combine this with both a raster-scanning microscope inside of a HOM interferometer and a quasiphoton number-resolving detection scheme [21].

## II. EXPERIMENTAL DETAILS

The target-entangled state in Eq. (2) is generated using a dual-Sagnac arrangement source that needs only one nonlinear down-conversion crystal, as shown in Fig. 2(a). A diagonally polarized CW 404 nm laser (linewidth  $\Delta\lambda < 5$  MHz; TOPTICA Photonics - TopMode 405) is split into two paths by a polarizing beam-splitter (PBS) pumping one 3-cm-long, type-II periodically poled potassium titanyl phosphate (ppKTP) crystal from two directions. Down-converted photon pairs centered at 808 nm are emitted from the ppKTP crystal in each direction, separated from the pump using shortpass dichroic mirrors (DMS) and subsequently interfere on a second PBS. The spatial mode is filtered with single-mode fibers at the output paths  $A$  and  $B$ .

In contrast to the polarization-entangled photon pair source designs based on a single Sagnac interferometer [22,23] or copropagating photon source designs based on two crystals in a crossed configuration [20], the generated photons in this system do not share a common path. As a result, the source is susceptible to phase instability of the parameter  $\phi(t)$  of the intended output entangled state Eq. (2) due to mechanical vibrations and temperature variations. To counter the sensitivity to phase in generating the required quantum state, we

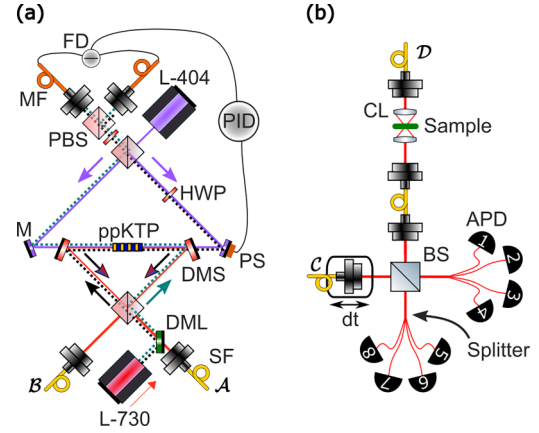


FIG. 2. Schematic of the wavelength-entangled photon pair source and HOM microscope. (a) Wavelength-entangled photon pair source, comprising a 404-nm CW pump laser (L-404), polarizing beamsplitter (PBS), mirror (M), half wave plate (HWP), periodically poled KTP crystal (ppKTP), piezoactuated mirror (PS), shortpass dichroic mirrors (DMS), longpass dichroic mirrors (DML), feedback controller (PID), fast balanced photodiode detectors (FD), two-meter length of single-mode fiber (SF2), multimode fiber (MF), and a CW laser at 730 nm to phase lock the source (L-730).  $A$  and  $B$  denote the two output modes from Eq. (2). (b) The HOM microscope, comprising lenses with focal length  $f = 11$  mm in a confocal configuration (CL), one-meter length of single-mode fiber (SF1), beamsplitter (BS),  $1 \times 4$  fused fiber coupler (Splitter), time delay for one input beam controlled by a translation stage (dt) and avalanche photodiode detectors (APD).  $C$  and  $D$  denote the input port of the interferometer. Any coincidences between one detector labeled among 1 to 4 with one detector labeled among 5 to 8 contribute to  $N_{11}$ , while any coincidences between pairs of detectors among 1 to 4 correspond to  $N_{02}$  and coincidences between pairs of detectors among 5 to 8 give  $N_{20}$ . This quasi-photon number resolving detection scheme adds an intrinsic loss of 25% for the bunching terms.

actively stabilize the setup using a diagonally polarized laser at the cutoff wavelength of the DMS (where these are only partially reflective) that is back-propagated through the source optics and monitored with fast balanced photodiode detectors. The subtracted electric signal from the photodiodes is sent to a PID controller that actuates a piezostack glued to the mirror of the clockwise pumping path.

The detuning of the central frequencies of the down-converted photons is readily controlled through phase-matching conditions, which in turn can be tuned by changing the crystal temperature while leaving the pump laser frequency unchanged. The temperature of the crystal can be set from 30°C to 180°C achieving a detuning from 0 to 30.1 THz (65.6 nm) (see Appendix B for the experimental characterization of the source). The photon pair source generates  $\sim 200$  k measured coincidences per second with an input pump power of  $\sim 20$  mW and we observe a symmetric heralding efficiency up to 25% at the positions marked  $A$  and  $B$  in Fig. 2(a).

The schematic of the confocal microscope is illustrated in Fig. 2(b). A semi-transparent sample (with a thickness  $d$  and refractive index  $n$ ) is mounted between two lenses in a confocal configuration in path  $D$ , before the broadband 50:50 beamsplitter (BS) where the HOM interference occurs. The presence of the sample introduces an additional time delay

between paths  $\mathcal{C}$  and  $\mathcal{D}$  related to the optical path length by  $t = nd/c$ . This changes the degree of indistinguishability between the two photons and consequently the relative number of antibunching events ( $N_{11}$ ) detected due to the HOM interference effect [12]. Depth features of the sample can also cause path-deviation of the probe photons, thereby altering the spatial overlap of the signal and idler modes at the BS. This reduces the visibility of the HOM interference leading to an error in the observed bunching rate and consequently in the sample thickness estimation. In our experiment we implement single-mode, raster-scanned imaging by translating the sample while keeping the probe beam fixed. A single-mode fiber after the sample implements spatial-mode filtering and ensures a constant overlap of the two spatial modes at the BS. Any change in detected coincidence rates due to the path-deviation or fluctuations in source brightness is normalized through the bunching events ( $N_{20}$  and  $N_{02}$ ) according to

$$P_{11} = \frac{\tilde{N}_{11}}{\tilde{N}_{11} + \tilde{N}_{02} + \tilde{N}_{20}}, \quad (3)$$

where  $\tilde{N}_{11}$ ,  $\tilde{N}_{02}$ , and  $\tilde{N}_{20}$  are calibrated via the Klyshko efficiency [24] (see Appendix C for the details). These values are all dependent on the HOM interference effect and are individually monitored with quasiphoton number-resolving detection scheme using multiplexed single-photon detectors [25,26] as shown in Fig. 2(b). As the HOM effect depends on the detection of coincident photons, all results in this paper estimating the thickness of the sample consider only photons which are postselected on successful detection. The detectors are silicon single-photon avalanche photodiode modules (APD; *Excelitas*) and the coincidences between them are recorded with a Logic16 time-tagger (*UQDevices*).

The transverse resolution of the microscope is limited by the beam waist of the scanning probe, while the axial resolution, which is the focus of this work, is given by the frequency of the beat note arising in the HOM interference. To maximize the Fisher information for the depth estimate while keeping all of the measurements within the same interference fringe half-period (avoiding fringe ambiguity), the signal and the idler photons are detuned by 7.4 THz (16 nm) giving a spatial beat note with a half-period  $\Delta/2 = 20.3 \mu\text{m}$ . For comparison to a classical linear optics approach, performing classical interferometry with an equivalent frequency of oscillation would require an electromagnetic radiation source with a central wavelength of  $\sim 40 \mu\text{m}$ . Operating at such a wavelength would constrain the transverse spatial resolution due to the diffraction limit. On the other hand, classical interference measurements operating at a similar wavelength to the down-converted photons ( $\sim 800 \text{ nm}$ ) will suffer from phase instability from the environmental background due to their high sensitivity.

### III. EXPERIMENTAL RESULTS

A test sample for imaging was fabricated by depositing micron-scale SU-8 polymer features with a thickness ( $10.62 \pm 0.02 \mu\text{m}$ ) onto a silica substrate (see Appendix D for the sample preparation) in the shape of a “KET” symbol [shown in Fig. 3(b)]. The thickness variation of the sample on a two-dimensional (2D) scan is shown in Fig. 3(a).

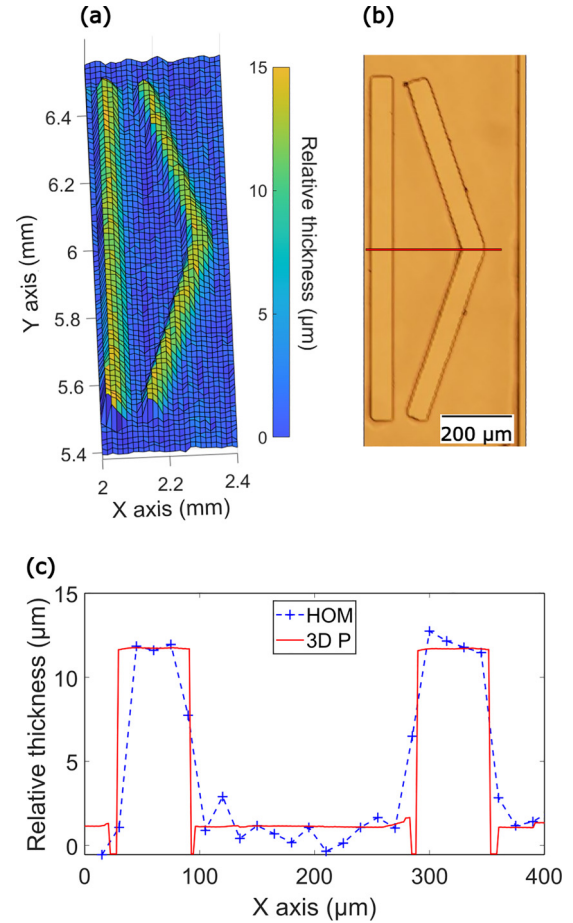


FIG. 3. Depth sample imaging. (a) 3D HOM imaging by monitoring the number of coincidences for each pixel. Raster scanning of the sample through the single-mode illumination provides the spatial resolution in the 2D transverse plane. The acquisition time is 0.5 s for each pixel ( $N \sim 4000$ ). The frequency beat note is 7.4 THz, where the detuning is chosen such that the characteristic depth features of this sample correspond to measurements across the full range of half of a fringe period from the HOM interference. This attains the maximum Fisher information while avoiding fringe ambiguity. (b) Two-dimensional conventional optical microscope image of the sample with a depth profile of  $(10.62 \pm 0.02) \mu\text{m}$  (see Appendix D for the sample preparation). (c) One-dimensional scan of depth profile following the path indicated by the red line on (b). Results are shown for HOM microscopy (blue) and for a 3D profilometer (red). See Supplemental Material for the raw data [31].

For initial calibration of the HOM microscopy system, the HOM interference features were measured for two pixels’ positions on the sample (with and without the deposited polymer) by translating the coarse delay in the reference arm (Fig. 4). Both measurements showed interference fringes with a visibility of  $\sim 80\%$ . The sample induces a relative time delay between the reference and the probe photons, leading to an offset of  $\sim 8 \mu\text{m}$  between the two interferograms. Assuming a sample refractive index of  $n = 1.58$  for the deposited structure, this corresponds to a measured thickness change of  $\sim 14 \mu\text{m}$ . For acquiring a full sample image this approach would be prohibitively slow due to the requirement of repeating the scan of a HOM interference fringe for every pixel.

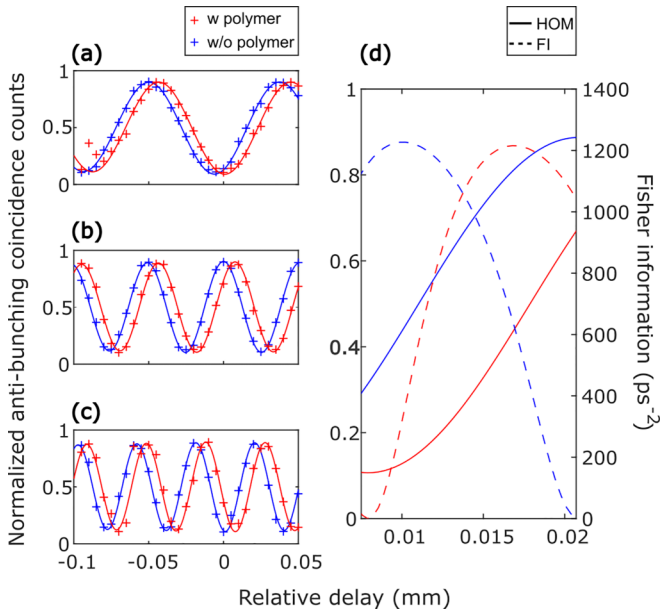


FIG. 4. Timing offset between interference fringes when comparing measurements at two pixels with different sample thickness. Comparison of the central regions of the HOM interference fringe patterns when applying different frequencies of the beat note: (a)  $\Delta\nu = 3.4$  THz, (b)  $\Delta\nu = 5.9$  THz, (c)  $\Delta\nu = 7.6$  THz. The blue markers and lines give the results for a selected pixel on the polymer deposition region of the sample and the red for a pixel in a region with only the substrate and no additional deposited material. Markers correspond to the measured data points and the lines are a numerical fit to a parameterised model of the interference. (d) Magnified view of a section of (c), with the associated Fisher information per photon shown as dashed lines for both measured positions on the sample. The coarse delay of the reference arm must remain within this range of relative delay to avoid fringe ambiguity. The Fisher information accounts for the intrinsic loss for the bunching terms given by the quasiphoton number resolution scheme used in this experiment. See Supplemental Material for the raw data [31].

Instead, the coarse delay is set at a fixed position within the range of 0.01 to 0.02 mm to avoid fringe ambiguity and the normalized antibunching coincidence counts are monitored for each pixel. The beat note is chosen to optimize the width of the Fisher information peak such that fringe ambiguity is avoided. Subsequently, the coarse delay is set at the crossing point for the Fisher information curves for the maximum and the minimum required depth measurement values. This provides a compromise by optimizing Fisher information and precision at both extremes of the measurement range. Finally, the relative time delay induced by the variation of the thickness within the sample is estimated through the variation in the probability outcomes  $N_{11}$ .

The phase-locking was monitored with an electronic data logger (Liquid Instruments, Moku:GO) to ensure stability of the photon pair source during the data acquisition. If failure in the phase-locking is detected, the system automatically suspends data acquisition and reacquires locking with a new set point for the PID controller. As this results in an unknown offset in the absolute value of the measured sample thickness, it is also necessary in this case to repeat the measurement of

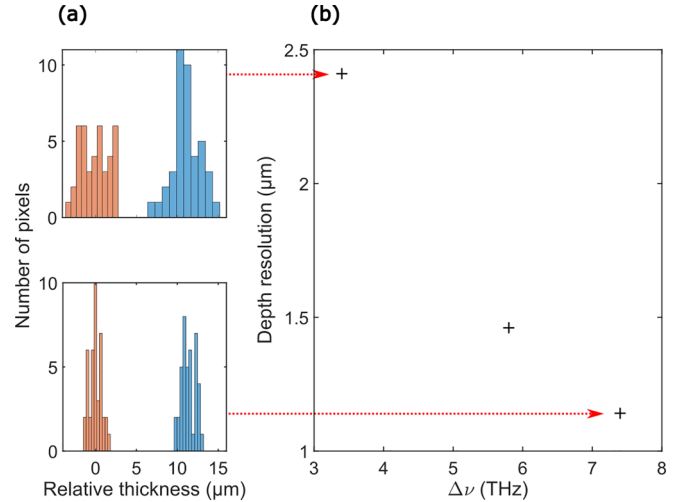


FIG. 5. Axial precision for varying beat note frequency. (a) Histograms of the axial depth estimate for the two-step measurement for beat note frequencies of 3.4 THz (top) and 7.4 THz (bottom). (b) Precision of depth estimation calculated from the raw histogram data using Eq. (4) after correction for the refractive index of the sample. See Supplemental Material for the raw data [31].

the previously acquired pixels. The outcomes of the HOM interferometer were measured for  $27 \times 78$  pixel positions, with data acquisition time  $\sim 20$  min ( $\sim 40$  min total measurement time due to the limited speed of the translation stages) for an area of  $0.4 \text{ mm}^2$ . The maximum transverse resolution of the HOM microscope was determined to be  $\sim 10 \times 10 \mu\text{m}^2$  with a resolution test target, but due to the size of this sample, a reduced transverse resolution ( $\sim 15 \times 15 \mu\text{m}^2$ ) was used to decrease the total acquisition time. Figure 3(c) shows a comparison of a one-dimensional (1D) raster scan across a single row of pixels using the HOM microscope with the results from a commercial three-dimensional (3D) profilometer (*Filmetrics - Profilm3D*)<sup>®</sup>. As the raster-scan pattern consisted of a vertical sweep in the  $Y$  axis followed by stepwise increment on the  $X$  axis, the 1D scan results correspond to data points monitored over a period of  $\sim 40$  min. The results from the HOM microscope agree with the measurements from the 3D profiler (within the given error of  $1.1 \mu\text{m}$  of the HOM microscope system) across the entire time period of the measurement. The sharpness of the edge features observed in the sample profile were limited for the HOM microscope measurement by the reduced transverse resolution. Assuming the known refractive index value for this polymer to be  $n = 1.58$  for both the signal and idler wavelengths, the measured relative thickness between the two steps in this sample is determined to be  $11 \pm 1 \mu\text{m}$ .

Figure 5 shows the results of repeated measurements of the sample for different beat note frequencies, which was used to characterize the axial precision. For each parameter combination, depth estimates were made by acquiring and combining data from groups of the same 40 pixels (a subset of a pixel column in the image). This was performed on two distinct regions of the sample, with one corresponding to pixels lying on the deposited polymer, which we denote as step 1 ( $S_1$ ), and the other on a region where no polymer was deposited,

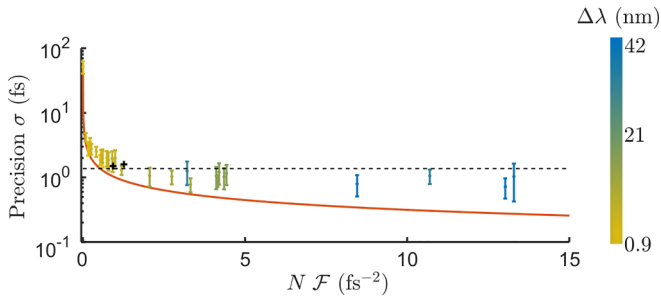


FIG. 6. Dependence of measured axial precision on total of Fisher information for single pixel estimation. Total Fisher information is given by the product of the number of detected photon pairs  $N$  and the theoretical Fisher information per photon  $\mathcal{F}$  [Eq. (1)]. Fisher information is controlled by varying the wavelength separation  $\Delta\lambda$  of the down-converted photons (color bar on right side). The acquisition time is fixed to 0.5 s and the number of detected photon pairs to  $N \sim 10^4$  for every data point. Each point on the graph corresponds to 500 independent time delay measurements split into blocks of 50, where the mean of the standard deviation of these blocks corresponds to the precision. The standard deviation from these ten blocks gives the error bars. The orange line corresponds to the theoretical bound of the precision for  $N$  photons saturating the Cramér Rao bound (CRB), and the two black crosses correspond to the two step measurement from Fig. 3(a). The horizontal dashed line is the threshold for achieving sub- $\mu\text{m}$  axial depth precision ( $\sigma < 1.4$  fs), given by Eq. (4) for a sample with a refractive index  $n = 1.58$ . See Supplemental Material for the raw data [31].

which is denoted as step 2 ( $S_2$ ). As the depth estimates for the two regions are statistically independent, the overall precision combining the two data sets is given by

$$\sigma_t = \sqrt{\text{var}(S_1) + \text{var}(S_2)}. \quad (4)$$

Figure 5(a) shows examples of the underlying histogram results of the measured depth for two of the data points in Fig. 5(b). The effect of increasing  $\Delta\nu$  is evident from the reduced variance of the data set of  $S_1$  and  $S_2$  arising from the increase in the Fisher information. Consequently the precision of the measurements is improved and smaller depth features can be more easily distinguished. The best precision result of 0.8  $\mu\text{m}$  for the relative sample thickness of each of the two steps individually leads to a combined precision of 1.14  $\mu\text{m}$  for the estimate of the relative depth offset between the two steps by using Eq. (4). In order to decouple thickness variation in the sample from the performance of the microscope, repeated measurements were performed on a single pixel. The normalized antibunching coincidence counts were measured 500 times for different frequencies of the beat note (from 0.09 THz to 18 THz). For each of the datapoints, the 500 measurements are split into 10 blocks of 50 measurements. The standard deviation of these ten blocks is calculated, giving a new dataset. The mean of each grouped dataset gives the precision value of the corresponding datapoint shown in Fig. 6 and the error bars are given by the standard deviation of the grouped datasets. In our laboratory the measurements were stable over a time period of  $\sim 40$  min and drift in the phase occurred over longer periods of time, which resulted from the mode-hopping instability of the laser used to phase-

lock the source. Changes in the output wavelength of the reference laser lead to fluctuations in the phase-locking conditions in the interferometer and drifts in the depth estimation. We also observe that as the Fisher information increases, the measured precision deviates from the CRB. We believe that this is due to an additional phase-locking instability observed at high crystal temperatures ( $\geq 120^\circ\text{C}$ ) causing perturbations in the refractive index. Two-color photon pair sources designed to be more robust to phase instability may provide an improvement in the saturation of the CRB for higher-frequency beat notes [20].

Using Eq. (4), it can be shown that sub- $\mu\text{m}$  precision can be achieved for a measurement with total Fisher information ( $N\mathcal{F}$ ) above  $0.5 \text{ fs}^{-2}$ . As shown on Fig. 6, this value is obtained with  $N = 10^4$  detected photon pairs and a detuning of 12.3 nm. The black crosses show the theoretical Fisher information and the precision achieved for each of the step measurements from Fig. 3(a). Therefore, sub- $\mu\text{m}$  precision for depth imaging would be expected for a source with the same detuning and twice the brightness.

#### IV. CONCLUSIONS

The total loss in the source and the microscope was relatively high ( $\sim 98\%$  for each photon). This included 6 dB of loss for FC to FC fiber connectors, which could be removed. This limited the total amount of Fisher information by reducing the number of detected probe photons for a given acquisition time. Reducing the loss and optimizing the brightness of the source could improve the axial resolution by an order of magnitude. To increase the precision further on more complex samples with greater thickness variations, while avoiding fringe ambiguity, one could perform an initial coarse mapping of the depth profile using raster scanning with a low-frequency beat note, followed by a scan at increased resolution with a larger wavelength detuning. High resolution scanning could also be reserved for targeted areas of interest to reduce the required measurement time.

We show that HOM interference can be implemented with two-color entangled photon pairs to achieve sub- $\mu\text{m}$  precision for depth estimation (approaching the performance of super-resolution microscopy) and with a probe light intensity of  $10^{-8} \text{ W/cm}^2$  incident on the sample. The dynamic range offered by measurement techniques of this type combined with sub- $\mu\text{m}$  axial precision could be particularly relevant for characterizing *in situ*, subcellular structures for semi-transparent samples such as biological cells.

#### ACKNOWLEDGMENTS

The authors are grateful to M. Piekarek, G. Ferranti, A. Belsley, and J. Rarity for helpful discussions. This work was supported by Engineering and Physical Sciences Research Council funded projects Nano-HOM (EP/R024170/1) QuantIC - The UK Quantum Technology Hub in Quantum Imaging (EP/T00097X/1). C.T. was funded by the EPSRC CDT in quantum engineering (EP/L015730/1). J.C.F.M. was supported by ERC starting grant PEQEM (803665). J.M.-R. would like to acknowledge funding from the EPSRC New Horizons Project No. EP/V048856/1.

### APPENDIX A: HONG-OU-MANDEL FOR TWO-COLOR STATE

With a type-II crystal and unfiltered, degenerate photon pair source, the probability of the antibunching state at the output from the HOM interferometer is modeled by [27]

$$P_{11}(t) = \begin{cases} 1/2[1 - \alpha(1 - |t/\tau|)], & \text{for } |t/\tau| \leq 1, \\ 1/2, & \text{for } |t/\tau| > 1, \end{cases} \quad (\text{A1})$$

where  $\alpha$  is the visibility of the HOM interference and is strongly dependent on the quantum-state visibility,  $t$  is the relative time delay between the two interfering photons, and  $\tau$  is the temporal width of the photons. Due to the type of the crystal and the absence of narrowband spectral filtering within the experimental setup, the down-converted photons ideally match the temporal shape of a top-hat function, with  $\tau = DL$ , where  $L$  is the length of the crystal and  $D$  is the difference between the inverse group velocities of the two down-converted photons [28,29].

To model the HOM interference of the two-color-entangled photons given by

$$|\Psi\rangle = \frac{1}{\sqrt{2}}(|\nu_S\rangle_A |\nu_I\rangle_B + e^{i\phi(t)} |\nu_I\rangle_A |\nu_S\rangle_B), \quad (\text{A2})$$

we multiply the term  $\alpha(1 - |t/\tau|)$  from Eq. (A1) by an additional term  $\cos[2\pi \Delta\nu t + \phi(t)]$  giving

$$P_{11}(t) = \frac{1}{2} \left[ 1 - \alpha \left( 1 - \left| \frac{t}{\tau} \right| \right) \cos[2\pi \Delta\nu t + \phi(t)] \right]. \quad (\text{A3})$$

$\Delta\nu = \nu_S - \nu_I$  is the frequency detuning between the signal and the idler and  $\phi(t)$  is the relative phase between the two substates from Eq. (A2). Due to conservation of energy, the probability of the bunching terms  $N_{02}$  and  $N_{20}$  is given in the ideal case by

$$P_{20} = P_{02} = \frac{1 - P_{11}}{2}. \quad (\text{A4})$$

### APPENDIX B: EXPERIMENTAL CHARACTERIZATIONS

The wavelength-entangled photon pair source has to be actively phase-locked to remove instability in the HOM interference, which otherwise results in noise in the measurement as shown in Fig. 7(a) [30]. To distinguish between changes in the brightness of the source and changes in the

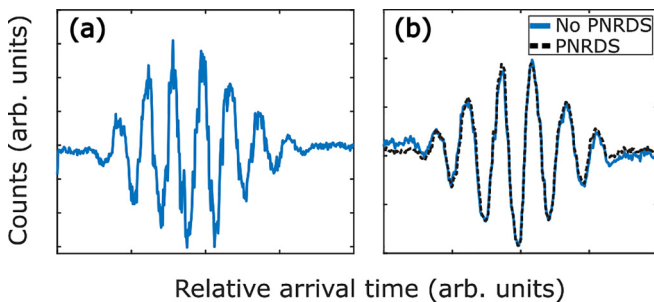


FIG. 7. Example of HOM interference stabilization. (i) No phase-locking or normalization, (ii) phase-locking and no normalization (blue), phase-locking and normalization with the use of PNRDS (dashed black).

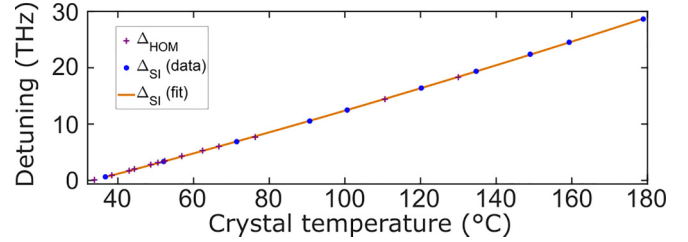


FIG. 8. Detuning of the photon pair. Blue data points are the experimentally measured values for detuning of the signal and idler peaks at different crystal temperatures.  $\Delta\nu_{\text{SI}}$  (yellow line) is a quadratic fit to these data points.  $\Delta\nu_{\text{HOM}}$  (purple crosses) shows expected values for the signal and idler detuning. These were calculated using Eq. (A3) from the frequency of the beat note of a measured HOM dip at each corresponding crystal temperature.

loss or bunching rate induced by the sample, the use of a quasiphoton number-resolving detection scheme (PNRDS) allows the bunching and antibunching terms to be monitored independently, normalizing the measurement. The effect of imbalanced alignment is apparent in Fig. 7(b) from asymmetry in the baseline count rate on the extreme right-hand and left-hand sides of the image (blue line), and is corrected by the use of the PNRDS (dashed black line).

Figure 8 shows characterization data for the frequency detuning between the signal and the idler of the photon pair source. The central wavelengths of the signal and idler peaks were measured with a sensitive, high-resolution spectrometer (*Andor, SR-750-B2-R-SIL*) for a range of crystal temperatures.

The pump laser wavelength was measured to be  $\lambda_p = 404.093$  nm with a linewidth of  $\Delta\lambda_p = 5$  MHz (Topmode 405, Toptica). As shown in Fig. 8, the detuning values predicted using the HOM interference beat note show good agreement with the calibrated detuning curve measured using the spectrometer.

### APPENDIX C: CALIBRATION WITH THE USE OF KLYSHKO EFFICIENCY

The calibration of  $N_{11}$ ,  $N_{20}$ , and  $N_{02}$  is implemented through the Klyshko efficiency [24]. We utilize the measured antibunching rate at a sufficiently large time delay to avoid HOM interference and define  $\eta_i$  to be the Klyshko efficiency of the  $i$ th channel ( $i = 1, 2, 3, 4$ ),

$$\eta_i = \frac{1}{4} \sum_{j=5}^8 \frac{C_{ij}}{2/3 S_j}. \quad (\text{C1})$$

$C_{ij}$  are the raw coincidence counts between the detectors  $i$  and  $j$ .  $S_j$  corresponds to the single counts detected by detector  $j$  ( $j = 5, 6, 7, 8$ ). With  $P_{11} = \frac{1}{2} = 2 \times P_{20} = 2 \times P_{02}$ , only  $2/3$  of the single counts from the detectors  $j$  will correspond to the state  $N_{11}$  while  $1/3$  of these single counts belong to the antibunching state  $N_{20}$ . Likewise, similar expressions can be derived for the other detector channels, where the roles of  $i$  and  $j$  are reversed. Finally, each coincidence count total  $C_{ij}$  can be normalized using the corresponding heralding efficiency coefficients to account for unbalanced losses.

## APPENDIX D: SAMPLE PREPARATION

The fabricated semi-transparent sample consisted of a 1-mm-thick fused silica substrate where a  $\sim 10\text{-}\mu\text{m}$ -thick film of a SU-8 polymer was deposited by spin-coating. SU-8 is a

negative epoxy photoresist with a high optical transparency, making it ideal for this work. Using photolithography, an image of a “KET” was transferred to the polymer, resulting in a semi-transparent sample with a variation thickness of  $(10.62 \pm 0.02)\text{ }\mu\text{m}$ .

- 
- [1] S. Slussarenko, M. M. Weston, H. M. Chrzanowski, L. K. Shalm, V. B. Verma, S. W. Nam, and G. J. Pryde, Unconditional violation of the shot-noise limit in photonic quantum metrology, *Nat. Photonics* **11**, 700 (2017).
- [2] T. Ono, R. Okamoto, and S. Takeuchi, An entanglement-enhanced microscope, *Nat. Commun.* **4**, 2426 (2013).
- [3] Y. Israel, S. Rosen, and Y. Silberberg, Supersensitive Polarization Microscopy Using NOON States of Light, *Phys. Rev. Lett.* **112**, 103604 (2014).
- [4] T. C. Ralph, N. K. Langford, T. B. Bell, and A. G. White, Linear optical controlled-NOT gate in the coincidence basis, *Phys. Rev. A* **65**, 062324 (2002).
- [5] H. F. Hofmann and S. Takeuchi, Quantum phase gate for photonic qubits using only beam splitters and post selection, *Phys. Rev. A* **66**, 024308 (2002).
- [6] J. L. O’Brien, G. J. Pryde, A. G. White, T. C. Ralph, and D. Branning, Demonstration of an all-optical quantum controlled-NOT gate, *Nature (London)* **426**, 264 (2003).
- [7] H.-S. Zhong, H. Wang, Y.-H. Deng, M.-C. Chen, L.-C. Peng, Y.-H. Luo, J. Qin, D. Wu, X. Ding, Y. Hu, P. Hu, X.-Y. Yang, W.-J. Zhang, H. Li, Y. Li, X. Jiang, L. Gan, G. Yang, L. You, Z. Wang *et al.*, Quantum computational advantage using photons, *Science* **370**, 1460 (2020).
- [8] C. K. Hong, Z. Y. Ou, and L. Mandel, Measurement of Subpicosecond Time Intervals Between Two Photons by Interference, *Phys. Rev. Lett.* **59**, 2044 (1987).
- [9] A. Lyons, G. C. Knee, E. Bolduc, T. Roger, J. Leach, E. M. Gauger, and D. Faccio, Attosecond-resolution Hong-Ou-Mandel interferometry, *Sci. Adv.* **4**, eaap9416 (2018).
- [10] N. Harnchaiwat, F. Zhu, N. Westerberg, E. Gauger, and J. Leach, Tracking the polarisation state of light via Hong-Ou-Mandel interferometry, *Opt. Express* **28**, 2210 (2020).
- [11] Y. Chen, Q. Shen, S. Luo, L. Zhang, Z. Chen, and L. Chen, Entanglement-Assisted Absorption Spectroscopy by Hong-Ou-Mandel Interference, *Phys. Rev. Appl.* **17**, 014010 (2022).
- [12] B. Ndagano, H. Defienne, D. Branford, Y. D. Shah, A. Lyons, N. Westerberg, E. N. Gauger, and D. Faccio, Quantum microscopy based on Hong-Ou-Mandel interference, *Nat. Photon.* **16**, 384 (2022).
- [13] M. Reisner, F. Mazeas, R. Dauliat, B. Leconte, D. Aktas, R. Cannon, P. Roy, R. Jamier, G. Sauder, F. Kaiser, S. Tanzilli, and L. Labonté, Quantum-limited determination of refractive index difference by means of entanglement, *npj Quantum Inf.* **8**, 58 (2022).
- [14] R. M. Woodward, B. E. Cole, V. P. Wallace, R. J. Pye, D. D. Arnone, E. H. Linfield, and M. Pepper, Terahertz pulse imaging in reflection geometry of human skin cancer and skin tissue, *Phys. Med. Biol.* **47**, 3853 (2002).
- [15] H. Chen, S. Ma, X. Wu, W. Yang, and T. Zhao, Diagnose human colonic tissues by terahertz near-field imaging, *J. Biomed. Opt.* **20**, 036017 (2015).
- [16] H. Yoo, J. Kim, and Y. H. Ahn, High-speed THz time-of-flight imaging with reflective optics, *Sensors* **23**, 873 (2023).
- [17] L. Schermelleh, A. Ferrand, T. Huser, C. Eggeling, M. Sauer, O. Biehlmaier, and G. P. C. Drummen, Super-resolution microscopy demystified, *Nat. Cell Biol.* **21**, 72 (2019).
- [18] K. Prakash, B. Diederich, R. Heintzmann, and L. Schermelleh, Super-resolution microscopy: A brief history and new avenues, *Philosophical Transactions of the Royal Society A: Mathematical, Phys. Eng. Sci.* **380**, 2220 (2022).
- [19] J. G. Rarity and P. R. Tapster, Two-color photons and nonlocality in fourth-order interference, *Phys. Rev. A* **41**, 5139 (1990).
- [20] Y. Chen, M. Fink, F. Steinlechner, J. P. Torres, and R. Ursin, Hong-Ou-Mandel interferometry on a biphoton beat note, *Npj Quantum Inf.* **5**, 43 (2019).
- [21] H. Scott, D. Branford, N. Westerberg, J. Leach, and E. M. Gauger, Beyond coincidence in Hong-Ou-Mandel interferometry, *Phys. Rev. A* **102**, 033714 (2020).
- [22] B.-S. Shi and A. Tomita, Generation of a pulsed polarization entangled photon pair using a sagnac interferometer, *Phys. Rev. A* **69**, 013803 (2004).
- [23] T. Kim, M. Fiorentino, and F. N. C. Wong, Phase-stable source of polarization-entangled photons using a polarization sagnac interferometer, *Phys. Rev. A* **73**, 012316 (2006).
- [24] D. N. Klyshko, Use of two-photon light for absolute calibration of photoelectric detectors, *Sov. J. Quantum Electron.* **10**, 1112 (1980).
- [25] D. Achilles, C. Silberhorn, C. Sliwa, K. Banaszek, I. A. Walmsley, M. J. Fitch, B. C. Jacobs, T. B. Pittman, and J. D. Franson, Photon-number-resolving detection using time-multiplexing, *J. Mod. Opt.* **51**, 1499 (2004).
- [26] G. Y. Xiang, B. L. Higgins, D. W. Berry, H. M. Wiseman, and G. J. Pryde, Entanglement-enhanced measurement of a completely unknown optical phase, *Nat. Photonics* **5**, 43 (2011).
- [27] Z.-Y. J. Ou, *Multi-Photon Quantum Interference* (Springer New York, 2007).
- [28] M. H. Rubin, D. N. Klyshko, Y. H. Shih, and A. V. Sergienko, Theory of two-photon entanglement in type-II optical parametric down-conversion, *Phys. Rev. A* **50**, 5122 (1994).
- [29] A. V. Sergienko, Y. H. Shih, and M. H. Rubin, Experimental evaluation of a two-photon wave packet in type-II parametric downconversion, *J. Opt. Soc. Am. B* **12**, 859 (1995).
- [30] The architecture of the photon pair source was chosen, in part, to avoid potential delay to a Ph.D. project that that was time-constrained during the COVID pandemic.
- [31] See Supplemental Material at <http://link.aps.org/supplemental/10.1103/PhysRevA.108.023726> for data used to generate figures in the paper.